

Journal of Materials Chemistry C

Accepted Manuscript

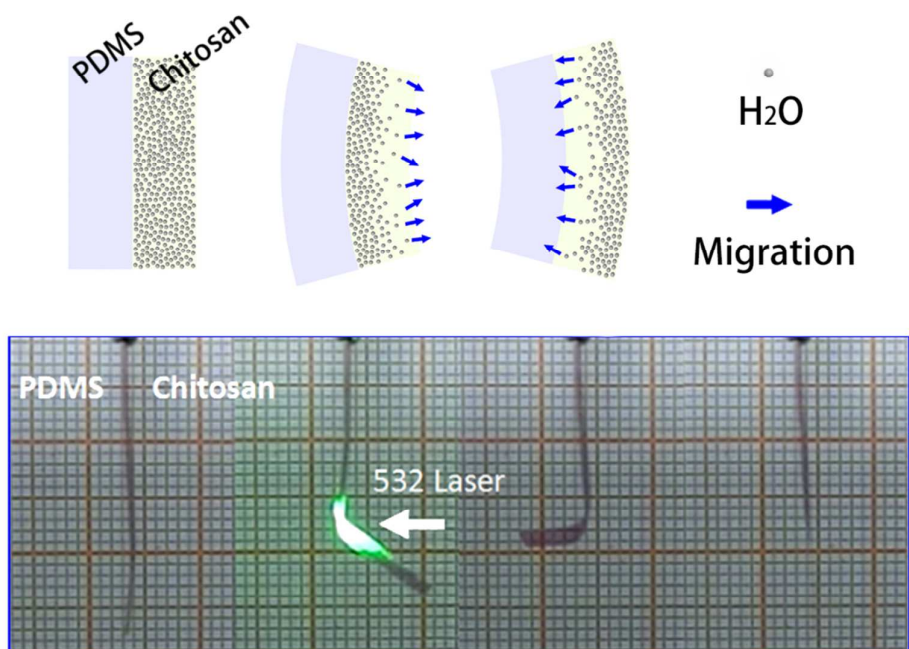


This is an *Accepted Manuscript*, which has been through the Royal Society of Chemistry peer review process and has been accepted for publication.

Accepted Manuscripts are published online shortly after acceptance, before technical editing, formatting and proof reading. Using this free service, authors can make their results available to the community, in citable form, before we publish the edited article. We will replace this *Accepted Manuscript* with the edited and formatted *Advance Article* as soon as it is available.

You can find more information about *Accepted Manuscripts* in the [Information for Authors](#).

Please note that technical editing may introduce minor changes to the text and/or graphics, which may alter content. The journal's standard [Terms & Conditions](#) and the [Ethical guidelines](#) still apply. In no event shall the Royal Society of Chemistry be held responsible for any errors or omissions in this *Accepted Manuscript* or any consequences arising from the use of any information it contains.



Low intensity responsive and wavelength-selective photothermal actuator based on dynamic mass transport process

COMMUNICATION

Wavelength-Selective and Rebound-able bimorph Photoactuator Driven by Dynamic Mass Transport Process

Cite this: DOI: 10.1039/x0xx00000x

Received 00th January 2012,
Accepted 00th January 2012T. Lan,^a Y. Hu,^a G. Wu,^a X. Tao^b and W. Chen^{*a}

DOI: 10.1039/x0xx00000x

www.rsc.org/

We fabricated wavelength-selective bimorph film photoactuators based on selective light absorption of Au nanocrystals. The dynamic mass transport of water in chitosan layer leads to ultra-sensitivity in respect of temperature and unique after-irradiation rebound behaviour. This work may provide new design strategy and performance promotion of photoactuators.

Photoactuation has great advantages on remote, contactless, non-electromagnetic disturbance and biotissue-permeable operation. Light plays the role of both energy source and control signal. Control commands can be programmed in size, shape, position and duration of light spot, as well as direction, wavelength, intensity and polarization of the beam. A series of efforts have been made to develop photoactuators based on various principles and strategies, especially photo-chemical-mechanical routes and photo-thermal-mechanical routes.¹⁻⁶ However, under the restrictions of low energy density and weak penetrability in material bulk, photoactuators have great challenge in device size and strain promoting.

In former studies, most attentions in photoactuation field were paid to liquid crystal elastomers (LCEs) and organic molecular crystals (OMCs).^{4,5} Both of them undergo photo-induced molecular isomerization, and are able to accumulate molecular scale deformation to macroscopic bulk deformation upon their anisotropic molecular assembly. Despite distinguished progresses have been made in above materials, the difficult molecular designs, syntheses and assemblies limit their cost reduction. We made efforts in nano-composite photoactuators for cost reduction and performance promotion, achieving preliminary results.⁶ However, the one-to-one correspondence wavelength-selectivity cannot be achieved with photochemical routes, because electrons can be excited by any light of shorter wavelength. The photothermal actuators can achieve one-to-one correspondence wavelength-selectivity through selective light

absorption. In order to achieve distinct selectivity, the wavelength differentials must be large enough (larger than 200nm by previous studies) to avoid the overlapping of absorption peaks. Thereby, remarkable temperature differentials trigger various heat-to-mechanical conversions, including thermal expansion, phase transition, shape memory and water loss, and the photothermal actuation is realized.^{1, 7-9}

Here we demonstrate a new type of photothermal actuator, which couples mass transport process to light-to-heat energy conversion. The light-to-heat energy conversion is offered by Au nanocrystals (AuNCs), which present wavelength-dependent high efficient photothermal conversion due to longitudinal surface plasmon resonance (SPR).^{3, 10} The peak wavelength depends on the aspect ratio of AuNCs, hence can be continuously tuned from green light (ca. 530nm) to infrared light. The AuNCs are doped in the chitosan layer of chitosan/polydimethylsiloxane (CS/PDMS) bimorph films. A heat-triggered directional water migration takes place in CS layer, inducing a stress gradient and subsequent film bending. Similar mass transport, driven by electric field, has already been well studied and contributes to deformation promotion.^{11, 12} Analogously, the photothermal actuation performance is significantly promoted with this mass transport process, presenting a nonlinear deformation growth with temperature. Therefore, the required temperature differential for selectivity is much smaller. Thus the absorption peaks can be partly overlapped and the wavelength spacing can be reduced to 100nm in our experiments. The performance is expected to be further promoted by better monodispersity of AuNCs.

Au nanoparticles (AuNPs) and nanorods (AuNRs) with different aspect ratio are synthesized according to reported methods and modified with sulfhydryl-terminated polyethylene glycol (mPEG-SH).¹³⁻¹⁵ The AuNCs-doped-chitosan films are fabricated through casting on glass slides and solvent evaporation. Then PDMS is casted onto the CS layer via spin coating method. Figure 1a

demonstrates the structure of the bimorph film. Au nanocrystals are uniformly doped in chitosan layer (CS, ca. 3 μm thick), modifying with sulfhydryl-terminated polyethylene glycol (mPEG-SH). Polydimethylsiloxane layer (PDMS, ca. 5 μm thick) covers one surface of the chitosan film. Table 1 lists the AuNCs doping species, peak wavelength and absorbance in the films. The three films are labelled **1** (peak wavelength 536nm), **2** (peak wavelength 635nm) and **3** (peak wavelength 772nm) respectively for convenience below. Figure 1b displays the transmission electron microscopy (TEM, FEI Tecnai G2 F20 S-Twin 200KV) images of the three kinds of AuNCs and their corresponding films. The variation of film colour intuitively indicates the wavelength-selective light absorption. Correspondingly, three common lasers, 532nm, 635nm and 808nm, are chosen to activate the films.

Table 1. AuNCs species, peak wavelength and absorbance in the films

Sample Number	Doping Species	Aspect Ratio	Absorption Peak in Films [nm]	Peak Absorbance
1	AuNPs	~1	536	0.434
2	Short AuNRs	1.95 \pm 0.32	635	0.405
3	Long AuNRs	2.84 \pm 0.16	772	0.347

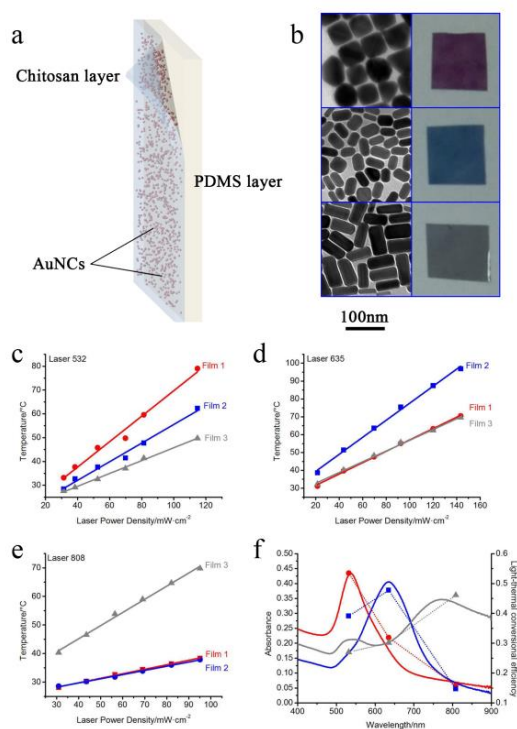


Figure 1. a. Demonstration of the bimorph actuator. b. TEM images of doping AuNCs and photos of bimorph films **1** (AuNPs, Pink), **2** (short AuNRs, Blue, AR 1.95 \pm 0.32) and **3** (Long AuNRs, Grey, AR 2.84 \pm 0.16). Photothermal conversion efficiency of each film with irradiation of c. 532nm laser, d. 635nm laser, and e. 808nm laser. f. Comparison of relative conversional efficiencies and absorbance of each film.

Photothermal properties of the films are characterized with infrared thermal imaging system (FLIR SC325) at room temperature and general environmental humidity (ca. 22 $^{\circ}\text{C}$, 20~40% RH). The highest temperatures that film **1**, **2** and **3** reach within 20s' irradiation of each laser and various intensities are plotted in figure 1c-e. The fitting straight lines' slopes reflect the light-thermal conversional efficiencies of these films. As expected, film **1**, **2** and **3** have highest photothermal conversion efficiency with 532nm, 635nm and 808nm laser respectively. The 532nm, 635nm and 808nm laser have highest heat output with film **1**, **2** and **3**, respectively, too. The relative values of photothermal conversion efficiencies are in well agreement with the light absorbance (Figure 1f).

To evaluate the actuation performance, the films are tailored into 25mm \times 2mm strips. The temperature is kept at room temperature, and humidity is kept among 22~40% RH. Shape changing is recorded by optical camera. Strip **1** bends toward the CS side upon 532nm laser stimuli (ca. 52mW $\cdot\text{cm}^{-2}$), indicating a relative volume change between chitosan layer and PDMS layer. When the laser ceases, the strip rapidly rebounds over the balance position and bends to the opposite side (Figure 2a). The rebound deflection angle is even larger than the during-irradiation deflection angle. The rebounding state lasts for about 10s before the strip starts to recover its initial shape. Such complex actuation behaviour has never been reported before in any other photoactuator.

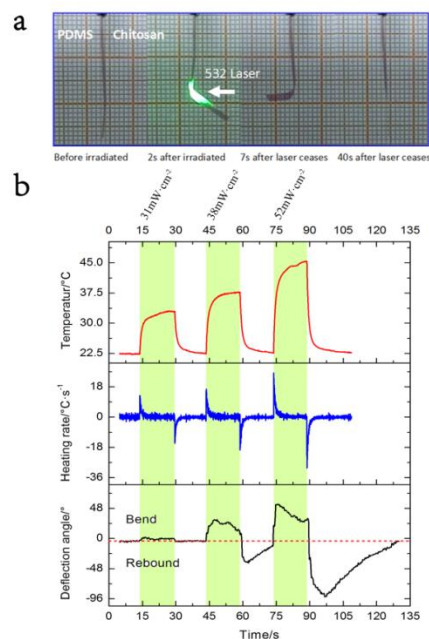


Figure 2. a. Photoactuation performance of strip **1** under laser 532. The strip bends for about 55 $^{\circ}$ within 2s' irradiation. After the irradiation ceases, it rebounds to the opposite side and reaches a maximum of -93 $^{\circ}$ in 7s, then the rebound bending decays within 40s. b. Synchronous temperature, heating/cooling rate and deflection angle curves of film **1** under laser 532 of 31, 38 and 52mW $\cdot\text{cm}^{-2}$.

Figure 2b shows the synchronous temperature, heating/cooling rate and deformation curve according to the infrared thermal imaging system and optical camera data (Movie 1). Strip **1** is irradiated by 532nm laser of increasing intensity. Under 31mW $\cdot\text{cm}^{-2}$ irradiation, the strip seldom bends upon irradiation nor rebound after laser ceases. When the laser intensity increases to 38mW $\cdot\text{cm}^{-2}$ in the next cycle, the during-irradiation deflection angle sharply increases

to about 30°. In addition, after the laser ceases, the strip rebounds for about -39° (negative value stands for reversed bending). Under 52mW·cm⁻² irradiation, the bending and rebound deflection angles reach 55° and -93°, respectively. During the meantime, however, the peak temperature only increases from 33.0 °C to 37.2 °C and 45.4 °C. It is a fairly small temperature range for such a huge deformation, even compared to heat-induced phase transition actuators. It is worth noticing that, both the bending and rebound deflection angles rapidly increase at first, reach a maximum and then slowly decrease. The increasing periods of deflection angle are more aligned with peaks of heating/cooling rate, rather than temperature, indicating that the dominated driving force is independent of temperature. The during-irradiation deflection angle decreases after the maximum, but never recovers the initial state, while the rebound deflection angle completely recovers within a long enough period, revealing a secondary effect of bimorph structure in this actuation.

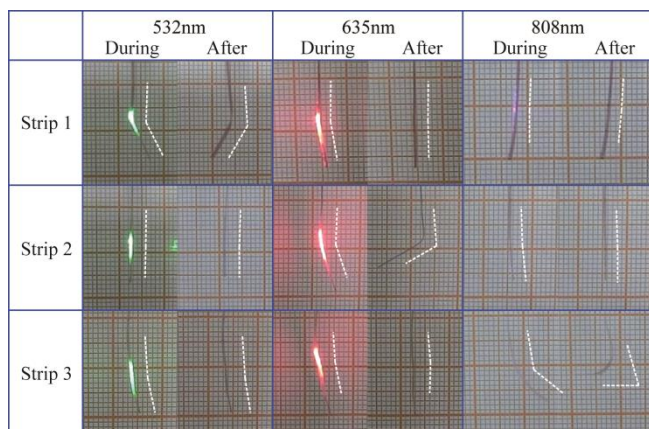


Figure 3. Wavelength-selectivity performances of strip 1, 2 and 3 under 532nm, 635nm and 808nm lasers (laser intensity is ~40mW·cm⁻²). Each strip bends and rebounds significantly under the corresponding laser, while seldom bend or rebound under non-correspondence laser. The wavelength-selectivity is demonstrated with the differences between during-irradiation bending and after-irradiation rebound.

The bimorph films doped with various AuNCs present distinct wavelength-selectivity with specific laser intensity. Figure 3 shows the during-irradiation bending and after-irradiation rebound of strip 1, 2 and 3 under 532nm (ca.40mW·cm⁻²) laser. These strips seldom bend nor rebound upon non-correspondence lasers. By contrast, the bending and rebound behaviour under correspondence laser is very significant. Overall, the differences of deflect angle, both during and after the irradiation, can represent wavelength-selectivity capacity of these actuators. The wavelength-selectivity can be achieved even the temperature difference is as small as 6 °C (32-38 °C) according to the measured light-to-heat conversional curves (figure 1b). Huge deformation at such low temperature and within such small temperature range is only reported in temperature-sensitive hydrogels (e.g. pNIPAm) which undergoes volume phase transition (VPT). Depending on the ultra-sensitive property, small-spacing (about 100nm) wavelength-selectivity can be realized with the partly overlapping absorption peaks of these actuators. In comparison, the wavelength spacing of wavelength-selective actuators is usually larger than 200nm in former studies because peak overlapping must be avoided to ensure large enough temperature differentials.

It is known that the coefficient of thermal expansion (CTE) of PDMS is 3.25×10⁻⁴K⁻¹.¹⁶ The CTE of CS is measured through thermal mechanical analysis (TMA) at room temperature and general relative humidity. TMA confirms that CS almost linearly contracts

among 28-43 °C (Figure S1). The calculated CTE of CS is -2.764×10⁻⁴K⁻¹. PDMS and CS layers deform in reversed ways when temperature varies, inducing a bending of the bimorph film. The deflection angle should be positively relative to temperature if the thermal expansion is the only reason for the bending, whereas the actuation curve in figure 2b suggests a more complex process.

Considering that chitosan is a hydrophilic polymer, the temperature changing may induce water loss and reabsorption. Therefore, the humidity influence is further measured. Figure S2 shows the humid-mechanical response of strip 1. The initially straight strip twists anticlockwise when placed into a glass flask containing desiccant, suggesting the water loss and contraction of CS layer. Then the strip is replaced into air, after what it strongly and immediately twists clockwise. In the following 22 seconds, the strip gradually recovers its initial shape. The humidity induced deformation process seems just similar to the photo induced bending and rebound, revealing that the light-to-mechanical energy conversion is accompanied with water loss and reabsorption. It is obvious that at each static state, such as figure S2 a, b and f, the strain is relatively small, while during the dynamic process (water reabsorption process), such as figure S2 c-e, the strain is extremely large. Though the lost and reabsorbed water quantity should be equal, the strain during the water loss process is much smaller than that during the reabsorption process.

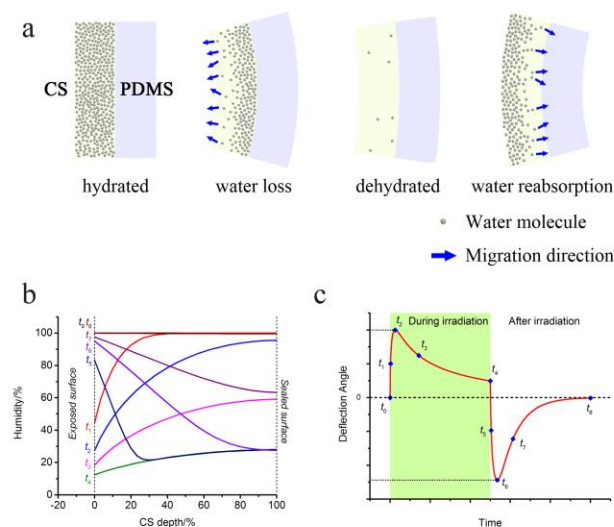


Figure 4. a. Demonstration of mass transport actuation mechanism. The water molecules are released during heating, thus an outward migration is generated. The humidity gradient and subsequent stress gradient induce the film bending. When the CS layer gets dehydrated, there is a much weaker bending due to relative volume changing between CS and PDMS. Reversed water migration happens during cooling process, and results in the rebound behaviour. b. Simulated humidity/strain distribution in CS layer at nine different stages: start (t_0), growth (t_1), maximum (t_2), decay (t_3), switch (t_4), rebound growth (t_5), rebound maximum (t_6), rebound decay (t_7) and end (t_8). Water is released at depth 0% and sealed at depth 100%. c. Simulated deflection angle-time curve and the corresponding points of t_0 - t_8 in a whole cycle.

To determine the influence of humidity, actuation performance of strip 1 is measured in dry air with irradiation of 532nm laser. The strip shows no remarkable deformation even the laser intensity increases to 180mW·cm⁻². Considering above evidence, it is reasonable to presume a dominated dynamic process. Generally, chitosan absorbs a small quantity of water molecules at room

temperature. Heating drives the water release of the films, which results in a contraction of chitosan matrix. However, water molecules can't permeate through the PDMS layer, thus the water exchange only takes place at the exposed surface of CS layer. The asymmetric migration from the sealed surface to the exposed surface will render a humidity gradient and subsequent stress gradient. The intra-CS stress gradient leads to a bending tendency of the CS layer. During the cooling stage, water molecules asymmetrically migrate from the exposed surface to the sealed surface, rendering a reversed humidity/stress gradient and bending tendency. Since the PDMS layer is extremely thin (5 μ m) and its Young modulus (2.04MPa) is 3 orders of magnitude smaller than that of CS (2.34GPa, 3 μ m), relative volume change between these two layers is not strong enough to dominate the bending. Overall, the intra-CS dynamic mass transport process induces the during-irradiation bending and after-irradiation rebound of the bimorph films (Figure 4a).

Numerical simulation applying finite elements method confirms the mass transport mechanism. The heating/cooling periods and inner temperature gradient are ignored in order to simplify the model. Moreover, there have been studies proving that the water migration in chitosan is governed by Fick's law within low humidity, and the Fickian diffusion coefficient increases in proportion to humidity in hydrophilic polymer.^{17, 18} In addition, it is reasonable to make below assumptions: First, surface water exchange rate is in proportion to surface humidity, and the interface layer, where the exchange takes place, is extremely thin compared to the entire CS layer; Second, the stress induced by water desorption and adsorption is in proportion to low humidity; Third, the CS matrix is governed by Hooke's law within the deformation range.

Based on above assumptions, figure 4b shows the simulated humidity distribution in CS layer along depth at different stages. It can be proved that the slope of fitting straight line of the humidity distributional curve is in proportion to the deflection angle. Therefore, the deflection angle-time curves can be simulated without consideration of bimorph bending (Figure 4c), too. The curves are in well agreement with the 3rd cycle in figure 2b. For the 3rd cycle, rebounding angle has slower growth, faster decay and larger amplitude than during-irradiation bending, just as same as the simulation. For the 1st cycle in figure 2b, mass transport is too weak to trigger a bending. The 2nd cycle is a transition from bimorph dominated bending to mass transport dominated bending. Bimorph bending in the 3rd cycle still effects on the actuation, resulting in the small difference between real actuation and the simulation. Overall, the simulation confirms the mass transport mechanism.

According to the mass transport mechanism, the deflection angle should be influenced by both thermodynamic and dynamic factors. For thermodynamic factor, higher temperature allows more water release/reabsorption and larger humidity gradient both during and after irradiation. For dynamic factor, surface water exchange rate grows faster with temperature than intra-CS diffusion rate does because the segment movement activation energy of chitosan is high. Once generated, the humidity/stress gradient spontaneously decays. Thus faster heating rate contributes to larger humidity/stress gradient. It is obvious that increasing of the chitosan thickness can reduce the temperature changing rate (by lower AuNCs density and slower heat dissipation) and weakens the humidity/stress gradient (dynamic factor), leading to a sudden disappearance of rebound phenomenon, which has been proved by further experiments (Figure S3). Coupling of these factors results in the rapid nonlinear growth (jump) of deflection angle. It is the utilizing of AuNCs (high efficient light-to-heat conversion) and embedded structure (heating from the inside)

cause a rapid heating and strong mass transport effect. Thus the film obtains the ultra-sensitivity to light and in consequence the small-spacing wavelength-selectivity.

Conclusions

In summary, we fabricated novel wavelength-selective photoactuator of AuNCs-doped-CS/PDMS bimorph films. The wavelength spacing is reduced to 100nm and is continuously tunable with aspect ratio of AuNCs. The actuation mechanism, which can be defined as dynamic mass transport coupled photothermal actuation, is quite different from any reported bistable photoactuator. Such photoactuator presents deflection angle jump among 33-38 °C, as well as unique rebound behaviour after irradiation ceases. The after-irradiation rebound is even stronger than the during-irradiation bending in a same cycle. The utilizing of AuNCs and embedded structure contribute to the ultra-sensitivity and wavelength-selectivity to light. Moreover, the mass transport mechanism may initiate a new class of photoactuator with improved performance.

Acknowledgements

This work was supported by the Natural Science Foundation for Distinguished Young Scientists of Jiangsu Province (BK2012008), the Hong Kong, Macao and Taiwan Science & Technology Cooperation Program of China (2012DFH50120), the National Natural Science Foundation of China (21373263, 11204350, 51303204), National Basic Research Program of China (2010CB934700), the External Cooperation Program of BIC, Chinese Academy of Sciences (121E32KYSB20130009), and the Natural Science Foundation of Jiangsu Province (BK20131173).

Notes and references

^a *i*-Lab, Suzhou Institute of Nano-tech and Nano-bionics, Chinese Academy of Science, Suzhou, 215123, China. E-mail: wchen2006@sinano.ac.cn

^b Nanotechnology Center, Institute of Textiles and Clothing, The Hong Kong Polytechnic University, Kowloon, Hong Kong SAR, P. R. China.

- X. Zhang, Z. Yu, C. Wang, D. Zarrouk, J.-W. T. Seo, J. C. Cheng, A. D. Buchan, K. Takei, Y. Zhao, J. W. Ager, J. Zhang, M. Hettick, M. C. Hersam, A. P. Pisano, R. S. Fearing, A. Javey, *Nature Communications*, 2014, **5**.
- B. Kundys, M. Viret, D. Colson, D. O. Kundys, *Nature Materials*, 2010, **9**, 803.
- Z. Zhu, E. Senses, P. Akcora, S. A. Sukhishvili, *Acs Nano*, 2012, **6**, 3152.
- S. Kobatake, S. Takami, H. Muto, T. Ishikawa, M. Irie, *Nature*, 2007, **446**, 778.
- F. Terao, M. Morimoto, M. Irie, *Angewandte Chemie International Edition*, 2012, **51**, 90.
- T. Lan, W. Chen, *Angewandte Chemie International Edition*, 2013, **52**, 6496.
- C. Li, Y. Liu, X. Huang, H. Jiang, *Advanced Functional Materials*, 2012, **22**, 5166.

- 8 D. J. Maitland, M. F. Metzger, D. Schumann, A. Lee, T. S. Wilson, *Lasers in Surgery and Medicine*, 2002, **30**, 1.
- 9 K. Nakata, Y. Ishikawa, M. Sakai, T. Ochiai, B. Liu, H. Sakai, T. Murakami, M. Abe, A. Fujishima, *Chemistry Letters*, 2011, **40**, 1229.
- 10 H. J. Chen, L. Shao, T. A. Ming, Z. H. Sun, C. M. Zhao, B. C. Yang, J. F. Wang, *Small*, 2010, **6**, 2272-2280.
- 11 T. Fukushima, K. Asaka, A. Kosaka, T. Aida, *Angewandte Chemie International Edition*, 2005, **44**, 2410.
- 12 G. Wu, G. H. Li, T. Lan, Y. Hu, Q. W. Li, T. Zhang, W. Chen, *J. Mater. Chem. A*, 2014, **2**, 16836-16841.
- 13 N. R. Jana, L. Gearheart, C. J. Murphy, *Langmuir*, 2001, **17**, 6782.
- 14 X. Ye, L. Jin, H. Caglayan, J. Chen, G. Xing, C. Zheng, D.-N. Vicky, Y. Kang, N. Engheta, C. R. Kagan, C. B. Murray, *Acs Nano*, 2012, **6**, 2804.
- 15 C. Fang, L. Shao, Y. Zhao, J. Wang, H. Wu, *Advanced Materials*, 2012, **24**, 94.
- 16 Y. Hu, W. Chen, *Macromolecular Chemistry and Physics*, 2011, **212**, 992.
- 17 S. Despond, E. Espuche, A. Domard, *Journal of Polymer Science Part B-Polymer Physics*, 2001, **39**, 3114.
- 18 S. Motupally, A. J. Becker, J. W. Weidner, *Journal of the Electrochemical Society*, 2000, **147**, 3171.